Optimizing Radar Scan Strategies for Observing Deep Convection

Using Observing System Simulation Experiments

Mariko Oue[1], Stephen M. Saleeby[2], Peter J. Marinescu[2,4], Pavlos Kollias[1,3], and
Susan C. van den Heever[2]

[1.] School of Marine and Atmospheric Sciences, Stony Brook University, Stony Brook, NY, USA
[2.] Department of Atmospheric Science, Colorado State University, Fort Collins, CO, USA
[3.] Environmental and Climate Sciences Department, Brookhaven National Laboratory, Upton, NY, USA
[4.] Cooperative Institute for Research in the Atmosphere, Colorado State University, Fort Collins, CO, USA

Correspondence to: Mariko Oue (mariko.oue@stonybrook.edu)

Abstract. Optimizing radar observation strategies is one of the most important considerations in pre-field campaign periods. This is especially true for isolated convective clouds that typically evolve faster than the observations captured by operational radar networks. This study investigates uncertainties in radar observations of the evolution of the microphysical and dynamical properties of isolated deep convective clouds developing in clean and polluted environments and aims to optimize the radar observation strategy for deep convection through the use of cloud-resolving model simulations coupled with a radar simulator and a cell tracking algorithm. Our analysis results include the following four outcomes. First, a 5-7 m s^{-1} median difference in maximum updrafts of tracked cells was shown between the clean and polluted simulations in the early stages of the cloud lifetimes. This demonstrates the importance of obtaining accurate estimates of vertical velocity from observations if aerosol impacts are to be properly resolved. Second, tracking of individual cells and using vertical cross section scanning every minute captures the evolution of precipitation particle number concentration and size represented by polarimetric observables better than the operational radar observations that update the volume scan every 5 min. This approach also improves the multi-Doppler radar updraft retrievals above 5 km AGL for regions with updraft velocities greater than 10 m s^{-1}. Third, we propose an optimized strategy which is composed of cell tracking by quick (1-2 min) vertical cross section scans from more than one radar in addition to the operational volume scans. We also propose the use of a single range-height indicator updraft retrieval technique for cells close to the radars, where the multi-Doppler radar retrievals are still challenging. Finally, increasing the number of deep convective cells sampled by such observations better represents the median maximum updraft evolution with sample sizes of more than 10 deep cells, which decreases the error associated with sampling the true population to less than 3 m s^{-1}.

1 Introduction

The quality and performance of remote sensing measurements, especially radar measurements, can strongly depend on the siting of instruments relative to their targets and the associated sampling strategies (e.g., Bousquet et al., 2008; Potvin et al., 2012b; Oue et al., 2019). This is especially true for convective storm systems that evolve rapidly over a range of spatial and temporal scales. The limitations associated with observation strategies influence microphysical, dynamical, and convective-core property retrievals, resulting in a misinterpretation of the observational data and can limit our understanding of storm processes. Some of these limitations can be addressed using Model and field Experiment data fusion (ModEx) concepts such as the optimization of experimental design using models and forward simulators. Using the ModEx framework, one can appropriately determine optimal radar deployments and scan strategies, as well as quantitatively understand the observational uncertainties arising from these strategies before field campaigns begin. As such, the goal of this study is to suggest optimal radar deployments and scan strategies for future radar field campaigns focused on convection.

In operational radar networks (e.g., the Next Generation Weather Radar (NEXRAD) network), each radar performs volume scans consisting of plan position indicator (PPI) scans with multiple elevation angles to prioritize collecting data for large areas. The volume scan strategy (known as volume coverage pattern, VCP) takes approximately 5 minutes to collect the 3D atmospheric data. While this operational scanning strategy is very valuable for performing surveillance and collecting a large number of cloud samples, it may not accurately capture fine-scale, rapidly-developing cloud phenomena. To increase our understanding of the links between convective cloud kinematic and microphysical processes, field campaigns have recently started to focus on collecting observations at higher temporal and spatial resolutions to understand fine scale characteristics and phenomena including isolated convection, shallow cumulus clouds, plumes embedded in mesoscale systems, and convective updrafts and downdrafts (e.g., Verification of the Origins of Rotation in Tornadoes Experiment 2 (VORTEX2), Wurman et al., 2012; Midlatitude Continental Convective Clouds Experiment (MC3E), Jensen et al., 2016; CSU Convective Cloud Updraft and Downdraft Experiment (C^{3}LOUD-Ex), van den Heever et al., 2021; Marinescu et al., 2020). Furthermore, in some of these field campaigns, physically tracking individual convective phenomena using cutting-edge radar systems was employed to prioritize high spatiotemporal sampling (e.g., The Dynamical and Microphysical Evolution of Convective Storms (DYMECS), Stain et al., 2015).

In recent years, as phased array weather radars have become more commonly used for severe weather observations, the sophisticated tracking of atmospheric phenomena has become feasible (e.g., Kollias et al., 2022), thus allowing for sampling of the entire cloud volume and cloud lifecycle. These observations are, however, more sensitive than previous approaches to scan strategies such as sampling time, azimuth/elevation spacings, and deployments (locations and the number of radars), all of which should be appropriately optimized depending on the spatial scale and evolution speed of the target phenomena (Kollias et al., 2020).

60   Several radar field campaigns aimed at enhancing our understanding of the links between convective cloud kinematic
61   and microphysical processes and life cycles have been planned for the near future (e.g., Tracking Aerosol Convection
62   Interactions ExpeRiment (TRACER), Jensen et al., 2019; Experiment of Sea Breeze Convection, Aerosols, Precipitation
63   and Environment (ESCAPE); Jensen et al., 2022; Atmospheric Radiation Measurements (ARM) Mobile Facility 3 (AMF3)
64   Southeast US deployment, Kang et al., 2021). All of these experiments plan to deploy multiple mobile weather radars, cloud
65   radars, and phased array radars. Optimizing the radar deployments and scan strategies while taking into account campaign
66   costs, deployment limitations, and sampling limitations (i.e., range, scan rate) is a large but critical challenge. In this paper
67   we make use of observing system simulation experiments (OSSEs) focused on deep convection to specifically investigate
68   the impacts of radar scan strategies on the cell tracking performance, microphysical evolution, and dynamical retrievals of
69   convective storms. Specifically, the impacts of varying the scan elevation angles, the period for a volume scan, and the
70   locations of the radars are assessed.

2 Method

72   Our OSSE approach is comprised of three parts: (1) the Regional Atmospheric Modeling System (RAMS; Cotton et al.,
73   2003; Saleeby and van den Heever, 2013); (2) the Cloud-resolving Radar Simulator (CR-SIM; Out et al., 2020); and (3) the
74   Tracking and Object-Based Analysis of Clouds (*tobac*; Heikenfeld et al., 2019; Sokolowsky et al., 2022). RAMS model
75   output from the Aerosol-Cloud-Precipitation-Climate (ACPC) model intercomparison project (MIP) (van den Heever et al.,
76   2018; Marinescu et al., 2021), which focuses on the development and occurrence of isolated convective cells in the region
77   around Houston, TX, on June 19-20, 2013 (Fig. 1a), form the basis of this study. The convective development is initiated
78   both along the inland propagation of the sea breeze, and later in association with convective cold pools produced by the
79   earlier convection in the simulation. In this study we focus on the time period from 20-24 UTC (15-19 local time) during
80   which period deep convective clouds developed, the dynamical processes of which have been extensively analyzed
81   (Marinescu et al., 2021). One-minute simulated deep convective fields are used as an input to CR-SIM to represent and
82   evaluate the radar observable fields (Fig. 1b). The CR-SIM radar observables are subsequently used to track convective
83   cells using *tobac*.

2.1 CR-SIM

85   CR-SIM is a sophisticated radar forward operator developed to bridge the gap between high-resolution cloud model
86   output and radar observations (Oue et al., 2020). CR-SIM can be applied to the 3D model output produced by a variety of
87   cloud-resolving models and large-eddy simulation models, including RAMS, the Weather Research and Forecasting (WRF,
88   Powers et al., 2017) model, the System for Atmospheric Modeling (SAM, Khairoutdinov and Randall, 2003), Cloud Model
89   1 (CM1, Bryan and Fritsch, 2002), and the Icosahedral Nonhydrostatic model (ICON, Zängl et al., 2015). It emulates the
90   interaction between transmitted polarized radar waves and rotationally symmetric hydrometeors and can simulate the power

91   (equivalent radar reflectivity factor), phase (Doppler velocity), and polarimetric (specific differential phase, differential

92   reflectivity, depolarization) variables with either a fixed elevation angle or varying elevation angles with respect to a

93   specified radar location. The radar simulator has been shown to be especially effective in OSSEs to investigate uncertainties

94   in observational data (Oue et al., 2019).

95   **2.2 *tobac***

96   *tobac* is a python-based software platform specifically developed for tracking atmospheric features, such as isolated

97   convective cells, in both model and observational datasets. *tobac* has been developed using a modular code structure with

98   data input, feature detection and segmentation, and trajectory linking steps. It uses a watershed algorithm to detect and track

99   individual convective cells, and it has been extensively tested on the ACPC simulations (e.g., Heikenfeld et al., 2019;

100 Marinescu et al., 2021). For this study, *tobac* is applied to CR-SIM vertically integrated liquid (VIL; Fig. 1c), which

101 represents the total hydrometeor condensate within each vertical column, and is similar to the approach used by Hu et al.

102 (2019). The CR-SIM radar reflectivity is converted into VIL using the following equation:

103 $VIL = \sum_{i=0}^{i=imax} \quad 3.44 * 10^{-6}[(Z_i + Z_{i+1})/2]^{4/7}(h_{i+1} - h_i) \quad [kg\ m^{-2}]$ (1)

104 where Z is radar reflectivity factor (mm^6 m^{-3}), h is height (m), i is the vertical index, and $i$max is the index at the grid

105 domain top. We calculate VIL using the CR-SIM-simulated total reflectivities greater than or equal to 0 dBZ at all vertical

106 levels and, thus, ensure that we consider all cloudy grid boxes in the tracking analysis. Although this variable is named

107 'liquid,' we use the total reflectivity from all modeled hydrometeor species to emulate real observations, including cloud

108 droplets, drizzle, rain, cloud ice, snow, aggregates, graupel, and hail. Since "VIL" is a widely-used name, we refer to VIL

109 as this parameter. When considering that clouds may have lower reflectivities (< 0 dBZ) and the radar minimum detectable

110 reflectivity increases with distance from the radar, the reflectivity threshold of 0 dBZ for the VIL calculation is a reasonable

111 value to use in detecting cells in the entire domain regardless of the distance. We also performed the cell tracking using 10

112 and 40 dBZ thresholds at the height of 2 km above ground level (AGL) to compare the performance of the use of VIL and

113 single-level reflectivity thresholds.

114 **2.3 RAMS**

115   RAMS is a cloud-resolving model that includes sophisticated microphysical-dynamical feedbacks, as well as aerosol-

116 cloud interactions (Saleeby and van den Heever, 2013). RAMS, along with several other cloud resolving models from

117 around the world participated in the ACPC MIP, focuses on the effects of changing the concentrations of cloud condensation

118 nuclei (CCN) on deep convective clouds (van den Heever et al., 2018). Case study simulations of a period of scattered

119 convective clouds near Houston, Texas were completed with relatively low and high concentrations of CCN that were based

120 on observations from the Houston area (see Figure 2 from Marinescu et al., 2021). The low-CCN simulation is initialized

121 with 500 cm^{-3} of CCN in the boundary layer (named CLN in this study), while the high-CCN simulation is initialized with

122 4000 cm^{-3} of CCN in the boundary layer (named POL in this study). The vertical aerosol profiles of both the CLN and POL

123   studies decrease linearly from the top of the boundary layer to 150 cm^{-3} at ~5 km AGL (the free troposphere), above which

124   they remain constant. RAMS allows for the advection, nucleation, wet and dry deposition, and regeneration of aerosol

125   particles via hydrometeor evaporation and sublimation. These simulations have been performed using a horizontal grid

126   resolution of 500m and RAMS' two-moment bin-emulating bulk-microphysics scheme, which predicts the mass and number

127   of eight hydrometeor types. The model data are output at a frequency of 1-minute. Additional details about the RAMS

128   model parameterizations and experimental setup used for these simulations can be found in Table 1 of Marinescu et al.

129   (2021).

2.4 Observation simulation processes

131   In this study, the cell tracking is applied to the CR-SIM-simulated radar observation field (VIL) to detect and track

132   individual convective storm cells. Using the tracking results for all cells, we investigate the performance of the cell tracking

133   using VIL and the impact of the scan strategy on the VIL estimates (Sect. 3.1) and the statistical impact of aerosols on the

134   cell dynamical evolution (Sect. 3.3). One of the tracked, isolated, deep convective cells with a single precipitation core is

135   chosen to investigate the following: 1) the impacts of the scan strategy on the examination of polarimetric observables and

136   related microphysical studies (Sect. 3.2); and 2) the influences of different sets of the scan strategies on the multi-Doppler

137   vertical velocity retrievals (Sect. 3.3).

2.4.1. Tracking convective cells

139   The *tobac* cell tracking is coupled with CR-SIM radar observables obtained using the RAMS model output in the

140   following manner:

141   1)   The RAMS model output from the ACPC MIP for an isolated convective case over the Houston area (Fig. 1a) is

142   used as an input to the CR-SIM runs;

143   2)   The radar observable fields (Fig. 1b) are simulated using CR-SIM;

144   3)   The CR-SIM simulated radar reflectivity is converted into VIL if the reflectivity exceeds 0 dBZ at all levels

145   (Fig.1c);

146   4)   *tobac* is applied to the VIL field to track the convective cells (Fig. 1d). We used the VIL thresholds of 0, 0.1, 1.0,

147   and 5.0 kg m^{-2} to identify/track individual cells, including those embedded in larger precipitation areas; and

148   5)   Apply steps 1-4 above to the CLN and POL RAMS simulations to investigate the impact of aerosols on the cell

149   dynamical evolutions in the entire simulation domain.

2.4.2. Emulating radar scan strategies

151   The various radar scan strategies emulated in this study are listed in Table 1. We first emulate cell tracking using sector

152   range-height indicator (RHI) scans, each of which is composed of full elevation angles from 0.5° to 89.5° with a 1° increment

153   in an azimuth sector and takes approximately 1 minutes (1-min RHI in Table 1). The 1-min RHI scan uses a snapshot of

154 data to complete a full elevation scan for a sector. The second emulation of cell trackings is also a full elevation scan for

155 an azimuth sector similar to 1-min RHI but takes 2 minutes using two continuous snapshots (2-min SEC); the first snapshot

156 is composed of angles from 0.5° to 44.5° over the elevation and the other is composed from 45.5° to 89.5° over the elevation

157 (we intended this simulation as 2-min "RHI" in which each of the two snapshots should be used for a half of the azimuth

158 sector for full elevation angles, however, for technical and computational reasons, we separated the elevation angles into

159 the two snapshots).

160 The sector scans for 1-min RHI and 2-min SEC follow an individual cell based on the results of the cell tracking using

161 *tobac*. Each azimuth sector is assumed to cover the 10-km width centered around the individual cells defined by *tobac*.

162 Therefore, the number of RHI sweeps for each cell varies as a function of the distance between the radar and the target cell.

163 The radar configuration for the RHI simulation is assumed to be a general scanning radar such as the ARM precipitation

164 radars. The angle range for an azimuth sector at the radar range of 40 km is approximately 14°.With the radar beam width

165 of 1°, the total beam for the sector scan is 90 (over elevation) x 14 (over azimuth) = 1260 beams. Assuming that each beam

166 uses ~96 radar pulse samples, the sector scan includes 120960 pulses in total. If the radar operates with 1.5 KHz pulse

167 repetition frequency (PRF) (typical value for C-band radars), then the sector scan takes 80 sec; and if the radar operates with

168 2.5 kHz PRF (typical value for X-band radars), then the scan takes 48 sec. These numbers (scans within 1-2 min) are easy

169 to get for phased-array radar observations. For a reflector radar that needs 33% overhead time due to acceleration and

170 deceleration of the antenna, these scan times become 106 sec and 64 sec respectively.

171 The second strategy we investigate is the 5-min VCP. This strategy follows the standard NEXRAD VCP precipitation

172 mode (VCP 12, https://www.weather.gov/jetstream/vcp_max) and is composed of 14 PPI scans. Since our model output is

173 every minute, for the 5-min VCP simulation, a volume scan is composed of 5 snapshots from the 1-min model outputs. A

174 single snapshot is used to create two or three PPI sweeps (two or three elevation angles).

175 Finally, we evaluate an "ideal" simulation where a volume scan with full elevation and azimuth scans with a 1.0°

176 increment over both elevation and azimuth is performed within 1-min (referred to as "Full" in Table 1). This approach will

177 be feasible when a network of rapid scan or electronically scanning radars is available. Although such observations are not

178 realistic, they can serve as an upper boundary in terms of observational capabilities and will be used for an evaluation of

179 VIL from 5-min VCP in Section 3.1.

180 We use an S-band frequency for the 5-min VCP simulation (emulating NEXRAD radars) and a C-band frequency for

181 1-min RHI, 2-min SEC, and Full simulations (assuming the C-band Scanning ARM Precipitation Radar (C-SAPR) , or any

182 equivalent performance radar). Since we use unattenuated radar observables in this study, the impacts of the radar frequency

183 on the simulation results should not be significant.

184

185 **2.4.3. Multi Doppler radar wind retrieval**

186   For the investigation of the impacts of scan and deployment strategies on multi-Doppler vertical velocity retrievals, this

187   study employs a three dimensional variational (3DVAR) multi-Doppler radar wind retrieval technique developed by North

188   et al. (2017). While this investigation focuses on uncertainties caused by scan and deployment strategies, it does not account

189   for other sources of errors such as attenuation, nor the particle fall speed assumed in the 3DVAR wind retrieval technique.

190   We use unattenuated radar reflectivity and reflectivity-weighted fall speed calculated by CR-SIM in the all present wind

191   retrieval simulations. The details of the 3DVAR retrieval settings are presented in Oue et al. (2019). As described in Oue et

192   al. (2019), the 3DVAR wind retrieval technique is applied to the gridded radar observable fields. The radar observables that

193   are resampled following the radar scan strategies in the previous sections are then regridded into a Cartesian coordinate of

194   250 km x 250 km x 14 km domain with 0.25-km horizontal and vertical spacings using Barnes distance-dependent

195   weightings (Barnes, 1964).

196

197   **3. Results**

198

199   **3.1 Uncertainty in tracking parameters**

200   Many previous convective cell tracking studies have employed reflectivity criteria at a given height (e.g., Steiner et al.,

201   1995; Shusse et al., 2006; Oue et al., 2014). This technique, however, can miss some of the early stages of convective cell

202   development that initiate at different (typical lower) heights. Figure 2a shows a comparison of the durations of *tobac*

203   detected and tracked cells in the CLN simulation as a function of the use of VIL, as well as 10 and 40 dBZ thresholds at 2

204   km altitude. The VIL-based tracking has the largest total number of cells detected since the VIL better captures the presence

205   of hydrometeor condensate throughout the vertical columns and is not dependent on the presence of condensate at a specific

206   level. All of the frequency distributions, perhaps unsurprisingly, peak at shorter durations for both CLN and POL cases. The

207   VIL-based and 10-dBZ-based tracking are more comparable, although the VIL-based tracking has higher frequencies at

208   even longer durations (> 90 min) compared to the 10-dBZ-based tracking. The 40-dBZ-based tracking generally has lower

209   frequencies at all duration time bins compared to the 10-dBZ- and VIL-based tracking, but it is more similar to the 10-dBZ-

210   based tracking in the 25-40 minute time bins. The frequency distributions of tracked cell lifetimes suggest that VIL can

211   better capture longer life cycles of individual cells, including their initial development and decay stages, due to its ability to

212   include information about hydrometeors in the entire column.

213   The POL simulation (dashed line in Figure 2a) shows a similar tracked cell lifetime distribution to the CLN case.

214   However, there are some notable differences. The POL case has fewer cells detected (~15% fewer), which is consistent with

215   Marinescu et al. (2021), who also found fewer deep convective updrafts in the POL case using different analyses (their

216   Figure 7). When considering the relative frequency distribution (not shown), the POL case also has a distribution shift

217   towards relatively fewer long-lived cells (lifetimes > 20 mins) and more frequent short-lived cells (lifetimes < 20 mins), as

218   compared to the CLN case. The relatively fewer long-lived cells in the POL case are associated with deep convection. There

219   could be several reasons for the difference in cell lifetimes related to microphysical-dynamical feedback processes, such as

220   those associated with cold pools (e.g., Grant and van den Heever, 2015). These differences between CLN and POL are being

221   examined in a separate manuscript. We, hereafter, use the CLN case to examine the effects of scan strategy on the radar

222   polarimetric observables and vertical velocity retrievals.

223   Since VIL integrates reflectivity from the surface to the observed echo top, it better captures hydrometeor condensate

224   in the entire vertical column. Conventional VCPs that do not include higher elevation angles or that have sparse elevation

225   scans, therefore, tend to produce an underestimation of VIL. Moreover, averaging inhomogeneities within large range-bin

226   volumes, which occur at distances far from the radar, can also cause uncertainties when using VIL. To assess these

227   uncertainties, we investigate the VIL as a function of distance from the radar.

228   Figure 3 compares contoured frequency by distance distributions of VIL from the 5-min VCP and Full scan (from 0°

229   to 90° over elevation) strategies. Although we use the horizontal distance from the radar instead of altitude in constructing

230   our contoured frequency by altitude diagram, we use the term 'CFAD' to refer to this kind of distribution diagram in this

231   study. Overall, both scans produce small differences in the frequency of less than 0.05 in the CFADs, except within the 30

232   km range from the radar. For 5-min VCP, there is a shift to higher frequencies of smaller VIL values (red color at distance

233   < 30 km and < -12 dB in Fig. 3b). At distances within 30 km of the radar, both radars have sufficient sensitivity (< -9 dBZ).

234   This underestimation is, therefore, likely due to the fact that 5-min VCP does not observe the upper parts of the clouds. The

235   smaller differences that occur at distances > 90 km, which are shown in both scan strategies, are likely due to the minimum

236   detectable reflectivity, which increases with distance from the radar. It can be concluded that even the NEXRAD VCP

237   captures the VIL well except for distances less than 30 km from the radar and is, thus, very valuable for the surveillance of

238   convective cells.

239

3.2 Evolution of polarimetric variables associated with microphysics

241   Polarimetric observables (e.g., differential reflectivity ZDR and differential propagation phase KDP) have frequently

242   been used by past studies as an indicator of microphysical and updraft evolution (e.g., Kumjian and Ryzhkov, 2008; Kumjian

243   et al., 2014; Snyder et al., 2013;). The NEXRAD' polarimetric measurements are very important for capturing the

244   precipitation microphysical properties, however, its poor spatiotemporal sampling (i.e., limited PPI elevation angles, time

245   for volume scan) provides only a limited view in convective storms (Fridlind et al., 2019). Here, we assess the impact of

246   the NEXRAD spatiotemporal sampling by simulating the polarimetric observables from the 1-minute RHI tracking (1-min

247   RHI in Table 1) and the 5-minute conventional PPI volume scan (5-min VCP in Table 1). We randomly select 12 cells from

248   the 453 deep convective cells tracked in the CLN simulation. These cells all have maximum radar reflectivity exceeding 45

249   dBZ and 20-dBZ echo top heights greater than 8 km AGL during their lifetime. We then examine the evolution of

250   microphysical and dynamical characteristics such as number concentration and mean diameter for each simulated

251   hydrometeor species, as well as the vertical velocity. Nine of the cells have 40-dBZ mean echo top heights that exceed the

252   freezing level (approximately 5 km AGL) and attain 8 km altitude, which signify stronger convection. These 9 cells show

253   similar evolution of K_{DP}, Z_{DR}, and maximum updrafts, all of which have magnitudes greater than 20 m s^{-1} in the middle of

254   their lifetimes. Three of the twelve cells do not have 40-dBZ echo top heights extending above the freezing level. From the

255   9 vigorous, deep convective cells, one cell is chosen for a detailed OSSE analysis based on its isolated nature and

256   development near the NEXRAD radar and other radar locations, planned for TRACER and ESCAPE. Figure 4 shows the

257   evolution of the mass-weighted mean diameter (D_m) and number density for the rain and hail species for the chosen cell.

258   Large rain D_m (> 1.5 mm) is evident near the freezing level during the later stage of the cell lifetime as the echo top height

259   descends (after 21:50 UTC in Fig. 4c). Around this time, the largest D_m for hail is also apparent (Fig. 4d). This indicates

260   that the large hail melts as it falls through the freezing level, thereby, producing large raindrops. The hail number

261   concentration (Fig. 4f) is also strongly correlated with updraft magnitude (Fig. 4b), thus, demonstrating the strong link

262   between the updraft dynamics and hail formation. Furthermore, the total hydrometeor mixing ratio (Fig. 4a) is consistent

263   with the number concentrations from both rain and hail (Figs. 4e and 4f).

264   Figures 5a,d,g (left column in Fig. 5) show simulated reflectivity, Z_{DR}, and K_{DP}, respectively, averaged over the region

265   with reflectivies > 40 dBZ from the original, cartesian model grid. The evolution of raindrops as represented by rain D_m

266   (Fig. 4c) is evident by the large values in the Z_{DR} field (Fig. 5d). The relatively large K_{DP} and reflectivity values also seem

267   to accurately represent the high number concentrations of rain in the early stage of the cell lifetime (Figs. 4e and 5a,g).

268   These characteristics of reflectivity, Z_{DR}, and K_{DP} are compared with those from the different scan strategies: 1-min RHI

269   (middle column) and 5-min VCP (right column). The RHI tracking reconstructs the magnitudes and evolution of the

270   polarimetric observables well (Figs. 5e and 5h) so that they represent the hail D_m and cell evolution (Figs. 4a,b,d).

271   Meanwhile, the conventional volume scan cannot capture the fine-scale structure and magnitudes of the hail-rain evolution

272   observed by Z_{DR} and K_{DP} (Figs. 5f and 5i) due to the coarse time resolution. The RHI tracking performs well in capturing

273   the K_{DP} enhancement and its streak as the raindrops fall (Fig. 5h). Note that the NEXRAD S-band frequency (3.0 GHz) is

274   assumed for the 5-min VCP simulation, while C-band frequency (5.5 GHz) is assumed for the model and RHI simulation.

275   Therefore, the K_{DP} values in this figure do include the frequency dependency. The S-band K_{DP} (Fig. 5i) is approximately

276   1.8 (5.5 GHz/3.0 GHz) times smaller than the C-band K_{DP} (Fig. 5h). This indicates that the K_{DP} measurements from the

277   shorter-wavelength radar are more sensitive to the K_{DP} evolution and therefore, can provide more insights on   the

278   microphysical evolution of precipitation.

279   **3.3 Dynamical evolution**

280   One of the benefits of cell tracking using VIL is that it can better capture the dynamical evolution of convective cells

281   over their lifetimes (Fig. 2). Figure 6 represents the maximum updrafts in the CLN and POL individual tracked cells as a

282   function of their lifetime for all of those deep convective cells in which their 20 dBZ echo top heights exceed the freezing

283 level. Many of the cells attain maximum updrafts > 10 m s⁻¹ within the first third of their lifetimes in both the CLN and POL

284 simulations. The peak occurrence for the POL simulation is found for updrafts that are approximately 5 m s⁻¹ stronger than

285 those of the CLN simulation, suggesting that stronger updrafts are more frequent in the POL than CLN convective cells in

286 the earlier stages of the cells' lifecycles. Since the earlier stages of convection are driven by warm-phase processes, this

287 finding is consistent with Marinescu et al. (2021), who found stronger updrafts in the warm-phase region of deep convective

288 updrafts, but not in the cold-phase region (i.e., above the freezing level) in the POL environment. The stronger updrafts

289 support the development of larger hail produced in the POL simulation (not shown). This result suggests that it is important

290 to estimate vertical velocity with a high level of accuracy if the impact of aerosols on convective dynamics is to be properly

291 resolved in observations. We use the CLN simulation outputs as well as the individual CLN case deep convective cell shown

292 in Figs. 4 and 5 to further investigate the uncertainties associated with the multi-Doppler radar vertical velocity retrievals

293 in this section. Figure 7 shows the maximum updraft velocity in the cell column at each time as a function of the normalized

294 lifetime for the nine deep convective cells from the CLN simulation selected in the previous section. They all have peak

295 updrafts exceeding 20 m s⁻¹, which mostly occur in the first half of the cells' lifetimes. The black line represents the profile

296 from the target cell analyzed for the OSSE in this section. It is clear from Figure 7 that the selected cell has a relatively

297 typical dynamical evolution when compared with the other nine cells, although it does reach its maximum updraft velocity

298 a little earlier in its lifecycle.

299   Figure 8 shows the impacts of sets of radar scan strategies for multi-Doppler updraft retrievals for the selected convective

300 cell using a 3DVAR technique (North et al., 2017; Oue et al., 2019). This cell is the same cell examined in the previous

301 section (Figs. 4 and 5). We simulate different combinations of the scan strategies using 1-min RHI that scans around the

302 center of the cell and 5-min VCP. Recall, Table 1 provides the details of the scan strategies, and Figure 1 shows the locations

303 of the radars with these scan strategies and the targeted OSSE cell. The sets of radars for the multi-Doppler wind retrieval

304 simulations are: 1) two radars, each using a 1-min RHI (red dot and cross in Fig. 1, called 2RHI); 2) two radars, each using

305 a 5-min VCP (called 2VCP); 3) two radars, with one using a 1-min RHI (red dot in Fig. 1) and the other using a 5-min VCP

306 (red cross in Fig. 1) (called RHIVCP); and 4) three radars, with two using 1-min RHIs (red and blue dots in Fig. 1) and one

307 using a 5-min VCP (red cross in Fig. 1) (called 2RHIVCP). Table 2 represents the root mean square errors (RMSEs) of the

308 retrieved vertical velocity at four different heights, as well as at all heights. The 2VCP simulation (Figure 8c; green in Figure

309 8f) significantly underestimates the updraft, with the error exceeding 5 m s⁻¹ above 5 km AGL, where the cell produces

310 mean updrafts stronger than 12 m s⁻¹. The 2VCP radar pair, whose volume scan takes 5 minutes, does not resolve the updraft

311 evolution well. We note that other studies also found an underestimation of vertical velocity retrievals using two 5-min

312 VCPs. For example, Marinescu et al. (2020) used two 5-min VCPs to estimate strong updrafts in supercells and found an

313 underestimation in the region from 5-10 km AGL when compared with radiosonde estimates of vertical velocity. This pair

314 of 5-min VCPs (2VCP) does, however, produce less error below 4 km AGL where the cell produces weaker updrafts (< 5

315 m s⁻¹) when compared with the other sets of radar combinations. This suggests that the conventional PPI scans, which have

316   dense scans at low elevation angles, well capture the low-level horizontal inflow, and the mass continuity assumption is

317   well satisfied at the low levels. It is interesting that while 5-min VCP represents VIL well for the distance > 30 km as shown

318   in Fig. 3, its limitations produce significant uncertainties in the convective dynamical retrieval of individual clouds above

319   ~5 km AGL even though the cell is observed at a distance > 30 km from the radar (Fig. 1).

320   With an RHI scan every minute, even when adding only one RHI, cell tracking improves the retrievals above 5 km altitude

321   (Figs. 8b,d,e; 2RHI, RHIVCP, and 2RHIVCP; red, magenta, and blue, respectively in Figure 8f). The improvements are

322   particularly significant for regions in which the updraft velocities are stronger than 10 m s⁻¹. The RHIVCP simulation shows

323   the best estimate at the middle altitude (~6 km) among the four simulations, followed by 2RHIVCP, and thirdly 2RHI. The

324   2RHI and 2RHIVCP simulations show RMSEs less than 6 m s⁻¹ at all altitudes and better estimates than the other two

325   simulations at the higher altitudes (8 and 10 km AGL). The RHI scan has better sampling in the higher elevations than 5-

326   min VCP, resulting in a better retrieval at these higher altitudes.

327   As the profile and Table 2 show, 2RHI and 2RHIVCP have the lowest RMSEs when considering all altitudes (Table 2,

328   bottom row). In addition, 2RHIVCP shows better results at altitudes < 10 km than 2RHI . This suggests that the conventional

329   5-min VCP scan can be used for further improvement of the RHI-only tracking retrievals for the low and middle altitudes.

330   Since the 5-min VCP has dense scans at lower elevations, this can help to provide enough data covering the horizontal

331   domain of the cell, which may better represent the low-level horizontal wind convergence, thereby, better constraining the

332   cost functions in the 3DVAR.

333   We also investigate the impacts of the radar radial locations relative to the same cell as in Figs. 4, 5 and 8. Radars

334   horizontally extending from 10 to 70 km (in 10 km increments) radially away from the cell are assessed. For this analysis,

335   we use the scan strategy with the lowest errors from our prior analysis, i.e., two radars performing 2-min SECs and one

336   radar performing 5-min VCP (e.g., Table 2, the tracking radars used 2-min SEC rather than 1-min RHI; we believe that 1-

337   min RHI can be feasible with electrical scan or mechanical rapid scan radars, but 2-min SEC can be sometime more

338   reasonable when the cell is relatively close to the radars and need to be scanned until higher elevations, as discussed in Sect.

339   2.4.2). Figure 9a shows the radar locations for the seven simulations and Figure 9b demonstrates the vertical profiles of

340   errors of the retrieved updrafts averaged over a 20 km x 20 km box with reflectivity > 30 dBZ at 21:42 UTC. For each

341   retrieval, the largest error is evident above an altitude of ~9 km AGL where the stronger updrafts are simulated by the model

342   (Fig. 8a). The largest error among the retrievals is found in the retrieval with the radars closest to the cell (red profile in Fig.

343   9b). This occurs since the PPI volume scan does not cover the upper part of the cell and/or the horizontal wind convergence

344   at higher elevation angles may not be retrieved from the RHI measurements accurately. When each radar has a distance

345   greater than or equal to 20 km from the cell, the retrievals are improved by 5-10 m s⁻¹ between 5 to 11 km altitudes. The

346   retrievals in which the radar distances from the cell fall between 20 and 50 km show errors less than 5 m s⁻¹ below 11 km

347   AGL. Such accuracies in the retrievals may allow for resolving the aerosol impacts on updraft velocities shown in Fig. 6.

348   The errors are then found to increase again above 10 km AGL, especially for the radars located 60 and 70 km away from

349 the cell. This investigation suggests that the radars should target cells that are between 20-50 km from the radar for optimal

350 multi-Doppler radar retrievals. This finding is consistent with previous field campaigns using multi-Doppler radar

351 measurements (e.g., Wurman et al., 2012; Collis et al., 2013; Jensen et al., 2016) and OSSE studies (e.g., Potvin et al.,

352 2012a).

353   In nature, convective cells often do not nicely evolve over pre-defined multi-Doppler regions and move outside the

354 region of optimal analysis. Therefore, we also propose a single-RHI vertical velocity retrieval which can be used on a much

355 larger sample of convective cells in the vertical in the vicinity of the radar compared to fixed, multi-Doppler platforms. The

356 single-RHI vertical velocity retrieval extracts the vertical air motion component from the radial velocity (Doppler velocity)

357 which is composed of the vertical air motion, horizontal air velocity, and hydrometeor fall velocity (Lamer et al., 2014). To

358 apply this technique to real observations, horizontal velocity and hydrometeor fall velocity should be provided. Generally,

359 the horizontal velocity profile can be provided from a velocity-azimuth display (VAD) technique using PPI measurements

360 or sounding measurements, assuming that the horizontal wind is constant at each level. However, this assumption is a major

361 source of the uncertainty in the single-RHI vertical velocity retrieval technique, particularly at lower elevation angles. At

362 these lower elevation angles, the horizontal wind component dominates the radial velocity, but the coverage of these lower

363 elevation angles often do not properly capture the variability in the horizontal wind, especially close to the radar. We

364 therefore investigate the impact of the distance of the radar from the cell on the single-RHI retrieval. In the simulations, we

365 use the reflectivity-weighted hydrometeor fall velocity simulated by CR-SIM, similar to the present multi-Doppler retrieval

366 simulations, to exclude the uncertainty related to the fall velocity estimates.

367   Figure 10 shows the simulated single RHI vertical velocity retrieval from the selected convective cell. Profiles in Figs.

368 10c and 10d are retrieved vertical velocity at the convective core (distance = 0 km) and the errors from the truth, respectively.

369 We investigate this technique for a profile at 21:42 UTC of the cell (same as Figs. 8f and 9b), where the strongest updraft

370 is simulated. This single-RHI Doppler velocity technique works very well at the distance = 0 km (red), where the horizontal

371 wind component can be ignored, as evidenced by the error profile being equal to 0 at all altitudes (red line). However, below

372 6km AGL, the error significantly increases with the radar distance from the core. Interestingly, the characteristics of the

373 error distribution are opposite to those of the multi-Doppler retrievals (Figs. 8f and 9b). We would, therefore, suggest the

374 complementary use of the multi-Doppler wind retrieval and the single-RHI vertical velocity retrieval for better vertical

375 velocity estimates of convective cells. For example, in a tracking strategy in which two radars track a targeted cell, the

376 optimal scenario can be one in which the two radars track the cell with sector RHI/PPI scans at intervals of ~2 min when

377 the distance of the cell from both radars is greater than 20 km. However, when the distance of the cell from one of the radars

378 is less than 20 km, the radar's scan is then switched to hemispheric RHI.

379   This study highlights the importance of focusing on high-spatiotemporal observations of individual convective cells

380 rather than utilizing conventional surveillance scans. Such high-spatiotemporal observations can be accomplished by

381 tracking cells using fast scan RHI measurements facilitated by rapid-scan radars. However, it is not hard to anticipate that

382 the number of individual cells tracked successfully during a short-term IOP period will also be limited. Therefore, we have

383   investigated the sample size of cells needed to represent the typical convective evolution of deep convective cells using the

384   median maximum updraft metric shown in Fig. 6. This specific analysis accounts for the error regarding cell sampling, but

385   it does not account for the wind retrieval uncertainty from the scan strategy. Figures 11a and 11c show boxplots of the

386   maximum vertical velocity as a function of the normalized lifetime from all convective cells detected (910 tracked cells

387   including deep and shallow cells) in the CLN case and from deep convective cells defined in Fig. 6a (453 tracked cells),

388   respectively. These figures indicate high variability in the maximum updraft magnitude as a function of time, and that

389   potentially, one randomly sampled convective cell may not represent the typical evolution of vertical velocity. Figure 11b

390   depicts the relationship between the sample size and the errors associated with estimating the full population median

391   evolution of the maximum updraft magnitude. We randomly sample convective cells from all of the *tobac*-detected cells in

392   the CLN simulation (910 tracked cells) and estimate the median value of maximum updrafts at each time bin with different

393   numbers of samples. The median values for the different sample sizes are then compared to the median values from the all

394   deep convective cells detected and shown as a black line in Fig. 6a to estimate RMSEs. Figure 11b suggests that increasing

395   the sample size generally decreases the RMSE to less than 4.5 m s^{-1} until a population of 10 cell samples is reached and

396   converges to approximately 2.6 m s^{-1} for a sample size of 20 or more samples. When focusing the analysis on deep

397   convective cells only (Fig. 11d), the RMSE decreases to approximately 3 m s^{-1} for 10 cell samples and converges to

398   approximately 1 m s^{-1} for 40 or more samples.

399   This study focuses on isolated deep convective cells, each of which has a single core. Although we provide a detailed

400   investigation of one selected cell using OSSEs, the result should be robust for the other cells that have a similar vertical

401   structure to that shown in Sect. 3.2. The error values presented in this study, however, may depend on cloud type. In

402   particular, as the larger errors of the multi-Doppler radar wind retrievals were shown to exist in the higher altitudes in this

403   study, the heights of convection could influence the observational uncertainties (i.e., height of maximum updraft). Moreover,

404   in a strong wind shear environment where storms advect quickly, the impact of the use of quick updates of RHI scans would

405   be more effective (e.g., Clark et al., 1980; Oue et al., 2019). Various convective cloud morphologies have been investigated

406   in terms of uncertainties in observations, including mesoscale convective systems (e.g., Bousquet et al., 2008; Oue et al.,

407   2019), supercells (e.g., Potvin et al., 2012; Marinescu et al., 2020), and convection embedded in stratiform precipitation

408   (e.g., Bousquet et al., 2008). However, the qualitative characteristics found in this study, such as the error profile trends, the

409   dependency on the radar locations, and the dependency on scan strategy, are likely to be common to those deep convective

410   cloud systems, as well.

411

4 Summary

413

414   Optimizing radar observation strategies has been one of the most important topics in pre-field-campaign periods,

415   especially when the focus is on atmospheric phenomena that rapidly evolve on timescales that standard operational radar

416   networks cannot resolve. This study uses the Cloud-resolving Radar Simulator (CR-SIM) and the *tobac* cloud object

417   tracking algorithm to investigate observational uncertainties of isolated deep convective clouds associated with pre-existing

418   and planned radar deployments and strategies. The focus of this manuscript is to optimize the radar observation strategies

419   for the TRACER/ESCAPE field campaign, but the results are generally applicable to all field campaigns focused on radar

420   observations of deep convection.

421   The following results and associated recommendations are made:

422   • The cell tracking algorithm works better with the use of VIL compared with the use of reflectivity thresholds at

423   individual altitudes to detect and track more convective cells for longer time periods, including the early-developing

424   and dissipating stages of isolated storms.

425   • An analysis of low-CCN (CLN) and high-CCN (POL) simulations, used to quantify the impact of aerosols on the

426   convective dynamical evolution, show a 5-7 m s^{-1} difference in maximum updraft at the early stages of convective

427   development. This suggests the importance of accurate vertical velocity estimates using the radar observations if the

428   impact of aerosols on convective updrafts is to be assessed. Fast scanning of the individual convective cells every

429   minute captures the microphysics and dynamics better than the operational radar observations that update the volume

430   scan every 5 min. The tracking of cells using RHI every minute better captures the evolution of K_{DP} in the early stage

431   and Z_{DR} in the later stage, which are primarily associated with the rain number concentration and hydrometeor particle

432   (hail and rain) size, respectively.

433   • Tracking using RHI improves the multi-Doppler radar updraft retrievals above 5 km AGL, particularly for regions

434   with updraft velocities greater than 10 m s^{-1}. The conventional 5-min PPI volume scan can be used for further

435   improvement of the RHI-tracking-only retrievals.

436   • The multi-Doppler radar updraft retrievals, even when using RHI, are still challenging, especially for cells that are

437   close to the radars (e.g., within 10 km of the radar). This approach can be complemented by a single RHI updraft

438   retrieval technique.

439   • Based on these results, the suggested best strategy to better capture microphysics and dynamics of deep convective

440   cells is tracking by frequent RHI scans from more than one radar (blue and red scans in Fig. 12), in addition to the

441   operational PPI volume scans generally performed by the NEXRAD radars (green scans in Fig. 12). We also suggest

442   a hybrid radar scan strategy which switches between the RHI cell tracking and hemispheric RHI measurements

443   depending on the distance between the radar and the targeted cell (red and orange scans in Fig. 12). Such RHI tracking

444   measurements would be possible with conventional mobile radars, but the fast-scanning Doppler radars (Wurman,

445   2001), and/or phased array radars (Kollias et al., 2022) would have more advantages in faster updating, better spatial

446   resolution, and higher quality datasets.

447   • Increasing the number of deep convective cells sampled by such observations better represents the population median

448   maximum updraft evolution. When increasing the number of deep cells sampled to more than 10, the RMSE

449   decreases to less than 3 m s^{-1}, and when increasing the sample size to more than 40, the RMSE further decreases to

450   less than 1 m s^{-1}.

451

452   Finally, this study highlights the importance of using OSSEs in developing radar strategies during pre-field campaign
453   periods. The use of a radar simulator in the OSSEs provides several advantages including 1) facilitating instrument
454   deployments such as the radar locations and the number of radars required; 2) optimizing radar configurations such as the
455   scan rate, elevation angles, update time of scans, and trade offs; and 3) quantifying errors of the observables and retrievals.
456   Effective OSSEs can lead to successful, state-of-the-art field campaigns and provide high-quality, unique datasets that can
457   allow for new insights of the atmospheric phenomena.

458

459
460   *Code availability*. The source code and user manual for the Cloud Resolving Model Radar Simulator (CR-SIM) are available
461   at https://www.bnl.gov/CMAS/cr-sim.php, last access: 21 April 2022, and those for Tracking and Object-Based Analysis
462   of Clouds (*tobac*) are available at https://tobac.readthedocs.io/en/latest/.

463

464   *Data availability*. The ACPC model intercomparison project deep convection simulation data used for the input of CR-SIM
465   are stored and can be accessed on the U.K. CEDA JASMIN supercomputer.

466

467   *Author contributions*. The radar simulator and cell tracking work and analysis were made by MO. Conceptualization of the
468   method, interpretation, and writing were shared between MO, PK, SMS, PJM, and SCV. The radar simulator was developed
469   by MO and PK's group, and the cell tracking code was developed by SCV's group.

470

471   *Competing interests*. The authors declare that they have no conflict of interest.

472

473   *Acknowledgements.*
474   M. Oue, S. M. Saleeby, and S. C. van den Heever were supported by Atmospheric System Research (grant no. DE-
475   SC0021160). M. Oue and P Kollias were also supported by National Science Foundation Grant FAIN-2019932.

476
477

478

References

Barnes, S. L.: A Technique for maximizing details in numerical weather map analysis, J. Appl. Meteorol., 3, 396–409, 1964.

Bousquet, O., Tabary, P., and Parent du Ch telet, J.: Operational multiple-Doppler wind retrieval inferred from long-range radial velocity measurements, J. Appl. Meteor. Climatol., 47, 2929–2945, https://doi.org/10.1175/2008JAMC1878.1, 2008.

Bryan, G. H., and Fritsch, J. M.: A benchmark simulation for moist nonhydrostatic numerical models. Monthly Weather Review, 130, 2917–2928, 2002.

Clark, T. L., Harris, F. I., and Mohr, C. G.: Errors in wind fields derived from multiple-Doppler radars: Random errors and temporal errors associated with advection and evolution, J. Appl. Meteorol., 19, 1273–1284, 1980.

Collis, C., Protat, A., May, P. T., and Williams, C.: Statistics of storm updraft velocities from TWP-ICE including verification with profiling measurements, J. Appl. Meteor. Climatol., 52, 1909–1922, https://doi.org/10.1175/JAMC-D-12-0230.1, 2013.

Cotton, W. R., and Coauthors: RAMS 2001: Current status and future directions. Meteor. Atmos. Phys., 82, 5–29, https://doi.org/10.1007/s00703-001-0584-9, 2003.

Kang, C., Giangrande, S.E., Serbin, S. P., Campbell, P., Hickmon, N., Ritsche, M. 2021: Science and Deployment Plan for the DOE 3rd Atmospheric Radiation Measurement Mobile Facility in the Southeastern United States, 2021 AGU Fall Meeting, New Orleans and Online, 13 – 17 December 2021, online available at https://www.arm.gov/uploads/2021_AGU_SE_US_TownHall_Slides.pdf

Fridlind, A. M., van Lier-Walqui, M., Collis, S., Giangrande, S. E., Jackson, R. C., Li, X., Matsui, T., Orville, R., Picel, M. H., Rosenfeld, D., Ryzhkov, A., Weitz, R., and Zhang, P: Use of polarimetric radar measurements to constrain simulated convective cell evolution: a pilot study with Lagrangian tracking, Atmos. Meas. Tech., 12, 2979–3000, https://doi.org/10.5194/amt-12-2979-2019, 2019.

Heikenfeld, M., Marinescu, P. J., Christensen, M., Watson-Parris, D., Senf, F., van den Heever, S. C., and Stier, P.: Tobac 1.2: Towards a flexible framework for tracking and analysis of clouds in diverse datasets. Geosci. Model Dev., 12, 4551–4570, https://doi.org/10.5194/gmd-12-4551-2019, 2019

Hu, J., Rosenfeld, D., Zrnic, D., Williams, E., Zhang, P., Snyder, J. C., Ryzhkov, A., Hashimshoni, E., Zhang, R., Weitz, R.: Tracking and characterization of convective cells through their maturation into stratiform storm elements using polarimetric radar and lightning detection, Atmospheric Research, 226, 192-207, 2019, https://doi.org/10.1016/j.atmosres.2019.04.015.

Jensen, M., Bruning, E., Collins, D., Fridlind, A., Kollias, P., Kuang, C., Rosenfeld, D., Ryzhkov, A., Varble, A., Brooks, S.D., Collis, S., Defer, E., Fan, J., Flynn, J., Giangrande, S., Griffin, R., Hu, J., Jackson, R., Kumjian, M., Logan, T., Matsui, T., McFarquhar, G., Nowotarski, C., Quaas, J., Oue, M., Sheesley, R., Snyder, J., Stier, P., Usenko, S., van den

512 Heever, S., van Lier Walqui, M., Wang, Y., Xu, Y., and Zhang, G.: Tracking Aerosol Convection Interactions
513   ExpeRiment (TRACER) Science Plan. Ed. by Robert Stafford, DOE/SC-ARM-19-017, 2019.

514 Jensen, M. P., Petersen, W. A., Bansemer, A., Bharadwaj, N., Carey, L. D., Cecil, D. J., Collis, S. M., Del Genio, A. D.,
515   Dolan, B., Gerlach, J., Giangrande, S. E., Heymsfield, A., Heymsfield, G., Kollias, P., Lang, T. J., Nesbitt, S. W.,
516   Neumann, A., Poellot, M., Rutledge, S. A., Schwaller, M., Tokay, A., Williams, C. R., Wolff, D. B., Xie, S., & Zipser,
517   E. J. (2016). The Midlatitude Continental Convective Clouds Experiment (MC3E), Bulletin of the American
518   Meteorological Society, 97(9), 1667-1686.

519 Jensen, M. P., Flynn, J. H., Judd, L. M., Kollias, P., Kuang, C., Mcfarquhar, G., Nadkarni, R., Powers, H., & Sullivan, J.
520   (2022). A Succession of Cloud, Precipitation, Aerosol, and Air Quality Field Experiments in the Coastal Urban
521   Environment, Bulletin of the American Meteorological Society, 103(2), 103-105.

522 Khairoutdinov, M. F., and Randall, D.A.: Cloud-resolving modeling of the ARM summer 1997 IOP: Model formulation,
523   results, uncertainties and sensitivities. J. Atmos. Sci., 60, 607-625, 2003.

524 Kollias, P., Luke, E., Oue, M., and Lamer, K.: Agile adaptive radar sampling of fast-evolving atmospheric phenomena
525   guided by satellite imagery and surface cameras. Geophysical Research Letters, 45, e2020GL088440.
526   https://doi.org/10.1029/2020GL088440, 2020.

527 Kollias, P., Luke, E., Tuftedal, K., Dubois, M. Knapp, E.J. : Agile Weather Observations using a Dual-Polarization X-
528   band Phased Array Radar. IEEE Radar Conference New York, NY.,2022.

529 Kumjian, M. R., and Ryzhkov, A. V.: Polarimetric signatures in supercell thunderstorms. *J. Appl. Meteor. Climatol.*, **47**,
530   1940–1961, doi:10.1175/2007JAMC1874.1, 2008

531 Kumjian, M. R., Khain A. P. , Benmoshe N. , Ilotoviz E. , Ryzhkov A. V. , and Phillips V. T. J.: The anatomy and physics
532   of ZDR columns: Investigating a polarimetric radar signature with a spectral bin microphysical model. *J. Appl. Meteor.*
533   *Climatol.*, **53**, 1820–1843, doi:10.1175/JAMC-D-13-0354.1. 2014.

534 Marinescu, P. J., Kennedy, P. C., Bell, M. M., Drager, A. J., Grant, L. D., Freeman, S. W.,, and van den Heever, S. C.:
535   Updraft vertical velocity observations and uncertainties in High Plains supercells using radiosondes and radars. Mon.
536   Wea. Rev., 148, 4435–4452, 2020, https://doi.org/10.1175/MWR-D-20-0071.1.

537 Marinescu, P. J., van den Heever, S. C., Heikenfeld, M., Barrett, A. I., Barthlott, C., Hoose, C., Fan, J., Fridlind, A. M.,
538   Matsui, T., Miltenberger, A. K., Stier, P., Vie, B., White, B. A., and Zhang, Y. : Impacts of Varying Concentrations of
539   Cloud Condensation Nuclei on Deep Convective Cloud Updrafts—A Multimodel Assessment, Journal of the
540   Atmospheric Sciences, 78(4), 1147-1172, 2021.

541 ModEx Approach - Environmental System Science Program, U.S. DOE Environmental System Science Program,
542   https://ess.science.energy.gov (accessed [May 11, 2022])

543 North, K. W., Oue, M., Kollias, P., Giangrande, S. E., Collis, S. M., and Potvin, C. K.: Vertical air motion retrievals in
544   deep convective clouds using the ARM scanning radar network in Oklahoma during MC3E, Atmos. Meas. Tech., 10,
545   2785–2806, https://doi.org/10.5194/amt-10-2785-2017, 2017.

546   Oue, M., Kollias, P., Shapiro, A., Tatarevic, A., and Matsui, T.: Investigation of observational error sources in multi-
547   Doppler-radar three-dimensional variational vertical air motion retrievals, Atmos. Meas. Tech., 12, 1999–2018,
548   https://doi.org/10.5194/amt-12-1999-2019, 2019.

549   Oue, M., Tatarevic, A., Kollias, P., Wang, D., Yu, K., and Vogelmann, A. M.: The Cloud-resolving model Radar
550   SIMulator (CR-SIM) Version 3.3: description and applications of a virtual observatory, Geosci. Model Dev., 13, 1975–
551   1998, https://doi.org/10.5194/gmd-13-1975-2020, 2020.

552   Potvin, C. K., Betten, D., Wicker, L. J., Elmore, K. L., and Biggerstaff, M. I.: 3DVAR versus traditional dual-Doppler
553   wind retrievals of a simulated supercell thunderstorm, Mon. Weather Rev., 140, 3487–3494,
554   https://doi.org/10.1175/MWRD-12-00063.1, 2012a.

555   Potvin, C. K., Wicker, L. J., and Shapiro A.: Assessing errors in variational dual-Doppler wind syntheses of supercell
556   thunderstorms observed by storm-scale mobile radars, J. Atmos. Ocean. Tech., 29, 1009–1025,
557   https://doi.org/10.1175/JTECHD-11-00177.1, 2012b.

558   Powers, J. G., Klemp, J. B., Skamarock, W. C., Davis, C. A., Dudhia, J., Gill, D. O., Coen, J. L., Gochis, D. J., Ahmadov,
559   R., Peckham, S. E., Grell, G. A., Michalakes, J., Trahan, S., Benjamin, S. G., Alexander, C. R., Dimego, G. J., Wang,
560   W., Schwartz, C. S., Romine, G. S., Liu, Z., Snyder, C., Chen, F., Barlage, M. J., Yu, W., and Duda, M. G. : The
561   Weather Research and Forecasting Model: Overview, System Efforts, and Future Directions, Bulletin of the American
562   Meteorological Society, 98(8), 1717-1737, 2017.

563   Rasmussen, E. N., J. M. Straka, , R. P. Davies-Jones, , C. A. Doswell, , F. H. Carr, , M. D. Eilts and , and D. R.
564   MacGorman,: Verification of the Origins of Rotation in Tornadoes Experiment: VORTEX. Bull. Amer. Meteor. Soc.,
565   75, 995–1006, 1994.

566   Shusse, Y., and Tsuboki, K. : Dimension Characteristics and Precipitation Efficiency of Cumulonimbus Clouds in the
567   Region Far South from the Mei-Yu Front over the Eastern Asian Continent, *Monthly Weather Review*, *134*(7), 1942-
568   1953.,

569   Stein, T. H. M., Hogan, R. J., Clark, P. A., Halliwell, C. E., Hanley, K. E., Lean, H. W., Nicol, J. C., and Plant, R. S.: The
570   DYMECS Project: A Statistical Approach for the Evaluation of Convective Storms in High-Resolution NWP Models,
571   Bulletin of the American Meteorological Society, 96(6), 939-951, 2015.

572   Steiner, M., Houze, R. A., Jr., and Yuter, S. E. : Climatological Characterization of Three-Dimensional Storm Structure
573   from Operational Radar and Rain Gauge Data, *Journal of Applied Meteorology and Climatology*, *34*(9), 1978-2007,
574   1995.

575   Wurman, J., Dowell, D., Richardson, Y., Markowski, P., Rasmussen, E., Burgess, D., Wicker, L., & Bluestein, H. B. :
576   The Second Verification of the Origins of Rotation in Tornadoes Experiment: VORTEX2, Bulletin of the American
577   Meteorological Society, 93(8), 1147-1170, 2012.

578   van den Heever, S. C., Grant, L. D., Freeman, S. W., Marinescu, P. J., Barnum, J., Bukowski, J., Casas, E., Drager, A. J.,
579   Fuchs, B., Herman, G. R., Hitchcock, S. M., Kennedy, P. C., Nielsen, E. R., Park, J. M., Rasmussen, K., Razin, M. N.,

580   Riesenberg, R., Dellaripa, E. R., Slocum, C. J., Toms, B. A., & van den Heever, A. : The Colorado State University
581   Convective Cloud Outflows and UpDrafts Experiment (C3LOUD-Ex), Bulletin of the American Meteorological
582   Society, 102(7), E1283-E1305.
583   Wurman, J.: The DOW mobile multiple-Doppler network. Preprints, 30th Int. Conf. on Radar Meteorology, Munich,
584   Germany, Am. Meteorol. Soc., 95–97, 2001.
585   Wurman, J., D. Dowell, Y. Richardson, P. Markowski, E. Rasmussen, D. Burgess, L. Wicker, H.B. Bluestein: The Second
586   Verification of the Origins of Rotation in Tornadoes Experiment: VORTEX2. Bull. Amer. Meteor. Soc., 93, 1147-
587   1170, doi: 10.1175/BAMS-D-11-00010.1, 2012.
588   Zängl, G., Reinert, D., Rípodas, P. and Baldauf, M. : The ICON (ICOsahedral Non-hydrostatic) modelling framework of
589   DWD and MPI-M: Description of the non-hydrostatic dynamical core. Q.J.R. Meteorol. Soc., 141: 563-579.
590   https://doi.org/10.1002/qj.2378, 2015.

591
592
593

594   Table 1. Radar scan strategies simulated in this study.

Strategy	Full elevation scan for an azimuth sector tracking cells (1-min RHI, 2-min SEC)	5-min volume coverage pattern (5-min VCP)	Full elevation/azimuth scan (Full)
Beam width	1.0°	0.9°	1.0°
Elevation angles	From 0.5° to 89.5° every 1°	0.48, 0.88, 1.32, 1.8, 2.42, 3.12, 4.0, 5.1, 6.42, 8.0, 10.02, 12.48, 15.6, and 19.51°	From 0° to 90° every 1°
Azimuth range	14.5° at 40 km radar range (Sector to cover a 10-km width centered around the individual cells with 1° spacing)	From 0° to 360° with a 0.5° increment	From 0° to 360° with a 1.0° increment
Time for volume scan	1 minute or 2 minutes*	5 minutes	1 minute

595   *With the radar beam width of 1°, the total beam for the sector scan is 90 (over elevation) x 14 (over azimuth) = 1260
596   beams. Assuming that each beam needs ~96 radar samples, the total number of pulses is 120960. This takes 1-2 min
597   with typical pulse repetition ratios (1.5 - 2.5 kHz) for C- and X-band radars. See detailed discussion in Sect. 2.4.2

598

599 Table 2. The root-mean-square error (RMSE) of the retrieved updraft averaged over the regions with reflectivity ≥40 dBZ
600 at four different altitudes as well as all heights for a variety of scan strategies for the entire lifetime.

	1. Two 1-min RHIs (2RHIs)	2. Two 5-min VCPs (2VCPs)	3. One 1-min RHI + one 5-min VCP (RHIVCP)	4. Two 1-min RHIs + one 5-min VCP (2RHIVCP)
10 km	4.794	16.82	7.995	4.800
8 km	5.371	7.396	5.609	5.112
6 km	5.862	6.601	4.764	4.895
4 km	4.232	3.178	3.625	3.511
All heights	5.030	6.763	5.539	4.535

601

602
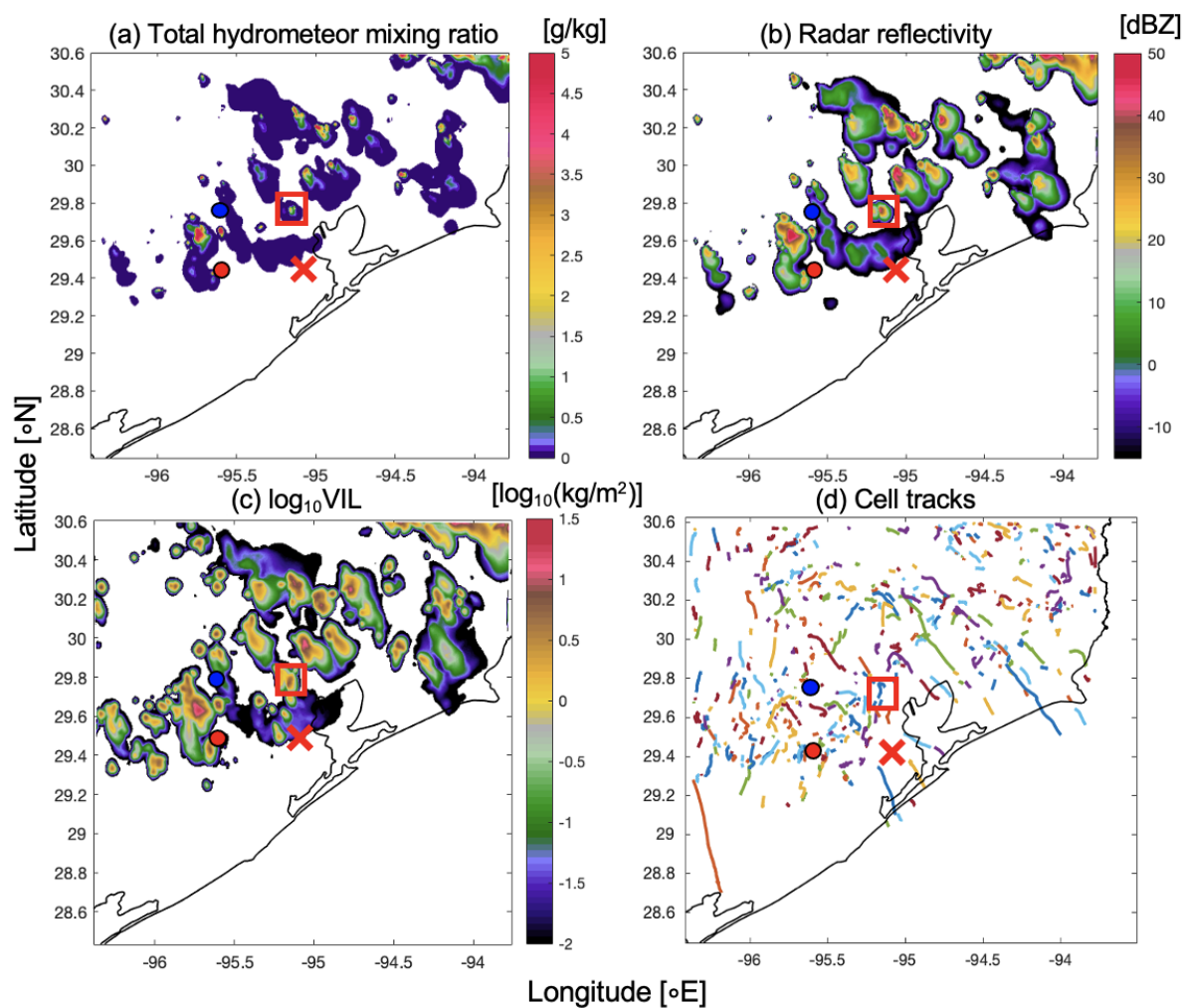
Fig. 1: (a) A snapshot of the RAMS-simulated total hydrometeor condensate field at 21:09 UTC at 5.5 km ASL; (b) CR-SIM simulated radar reflectivity field at the same height and same time as (a); (c) vertically integrated liquid (VIL) estimated from the CR-SIM C-band total reflectivity (from total liquid and ice hydrometeor condensate) at the same time as (a); and (d) tracks of precipitating convective cells detected between 20:00 and 23:59 UTC using *tobac*. On each panel, the red "X" marks the location of a radar performing 5-min VCP (i.e., NEXRAD KHGX), the red solid dot represents the location of a radar performing a different 5-min VCP or RHI, and the blue solid dot represents the location of another radar performing RHI. The red rectangle represents the tracked cell of interest used for multi-Doppler radar retrieval and polarimetric evolution analysis.
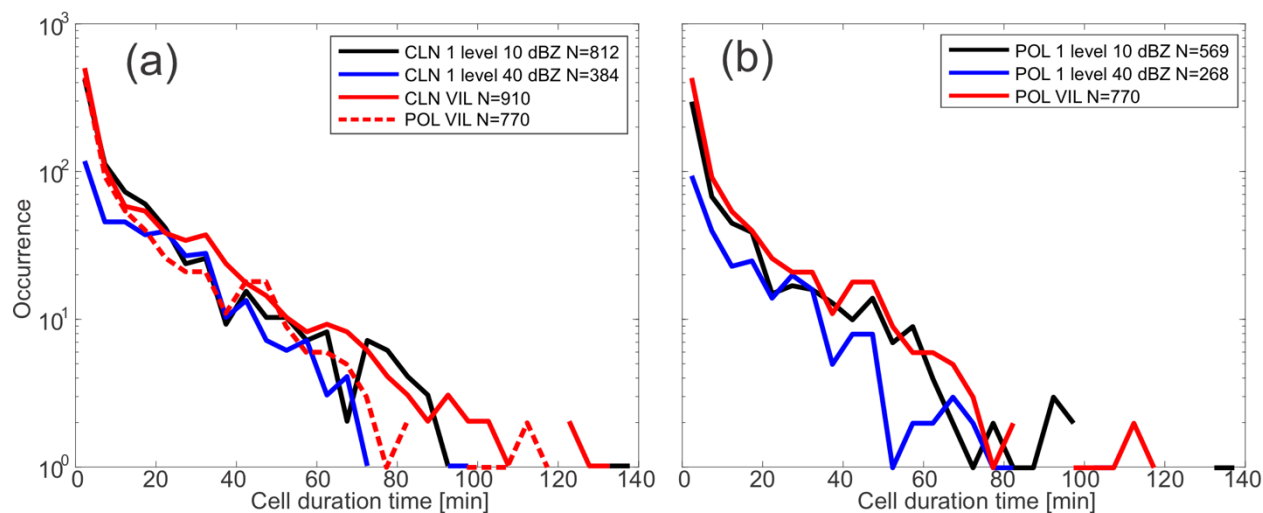
Fig. 2: Frequency distributions of cell duration time from the *tobac* cell tracking using VIL (red), 10 dBZ threshold at 2 km height (blue), and 40 dBZ threshold at 2 km height (black) for (a) CLN and (b) POL cases. The legend displays the total number of detected cells (N) for each tracking parameter utilized. Panel (a) also includes the cell tracking using VIL for the POL case shown as the red dashed line.
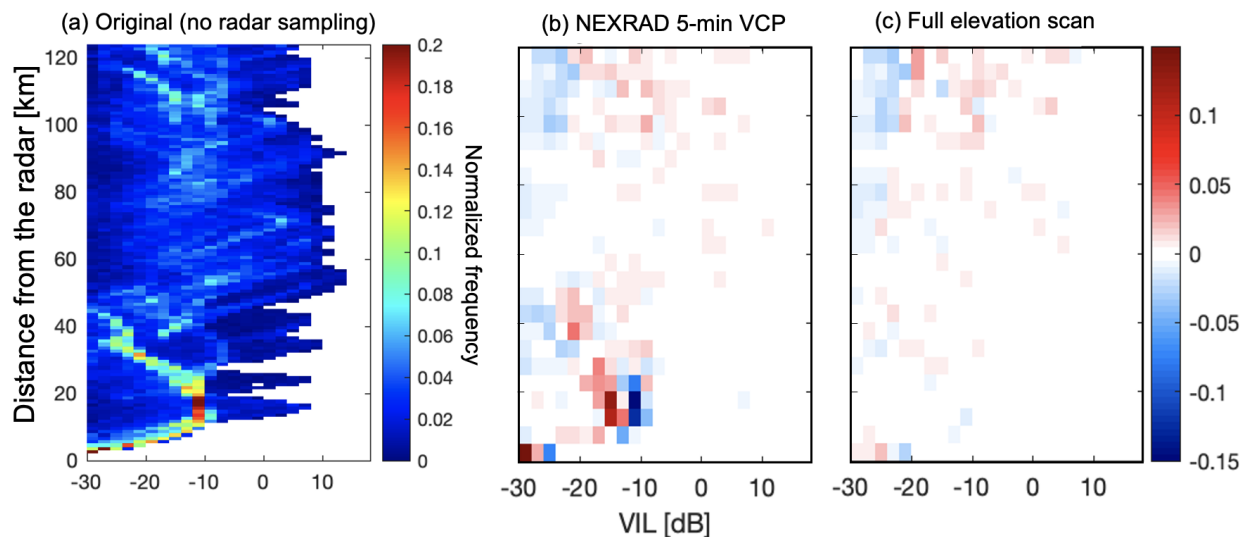
Figure 3: (a) Contoured frequency by distance (from the radar) distribution of the VIL from the original, cartesian model grid from the 1-minute output over the 4-hour analysis time period; (b) difference between the VIL from the 5-min VCP scan strategy and (a); and (c) difference between the VIL from the Full scan strategy and (a). The VILs from the 5-min VCP and Full scan strategies are estimated from the gridded reflectivity fields with 250 m horizontal and vertical spacing and 1-minute output over the 4-hour time period.
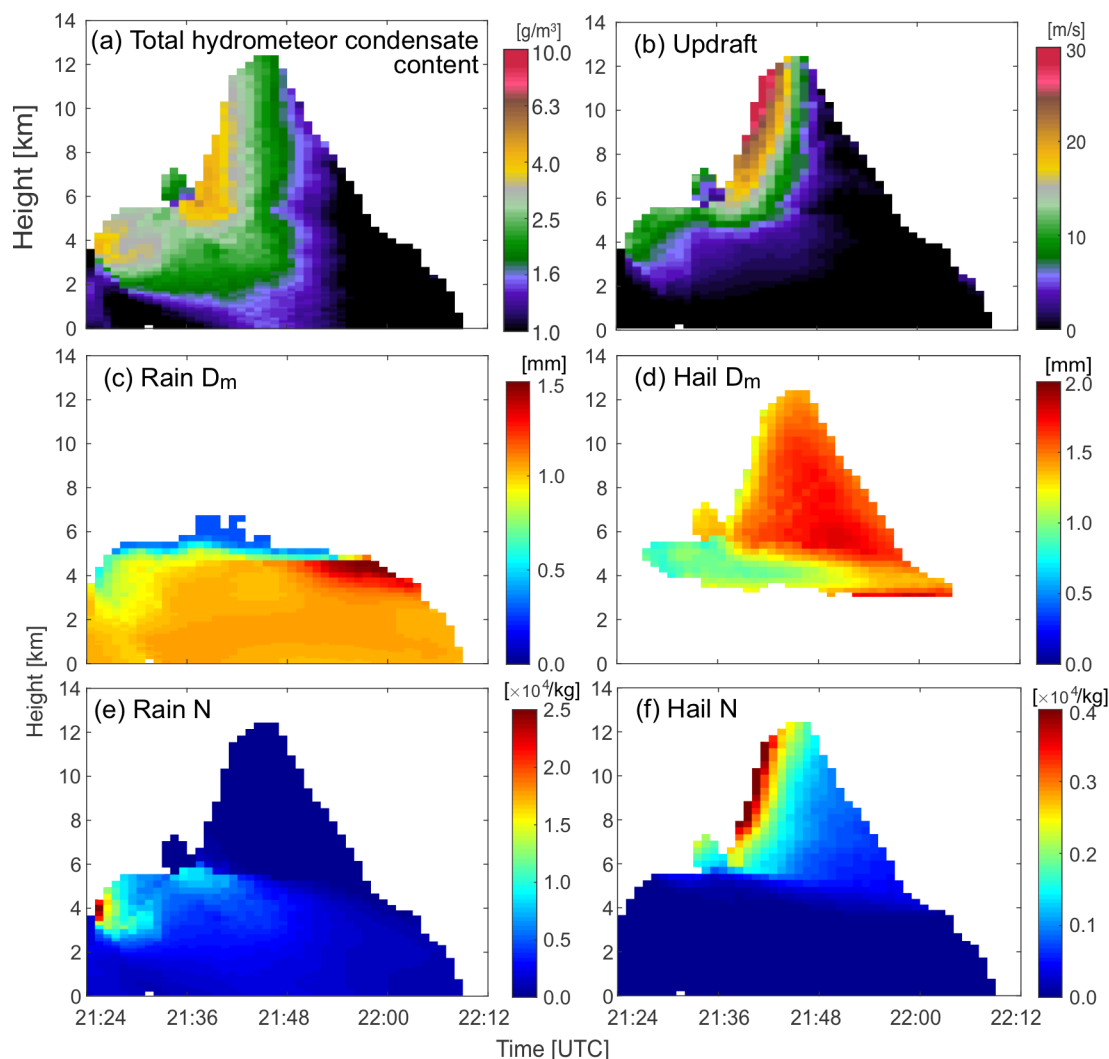
Fig. 4: Height-versus-time cross sections of the (a) total hydrometeor condensate content, (b) updraft, (c-d) the mass-weighted mean diameter (D_m) for (c) rain and (d) hail, and the number density (N) for (e) rain and (f) hail, averaged for areas with reflectivity > 40 dBZ of the selected convective cell from the CLN case.
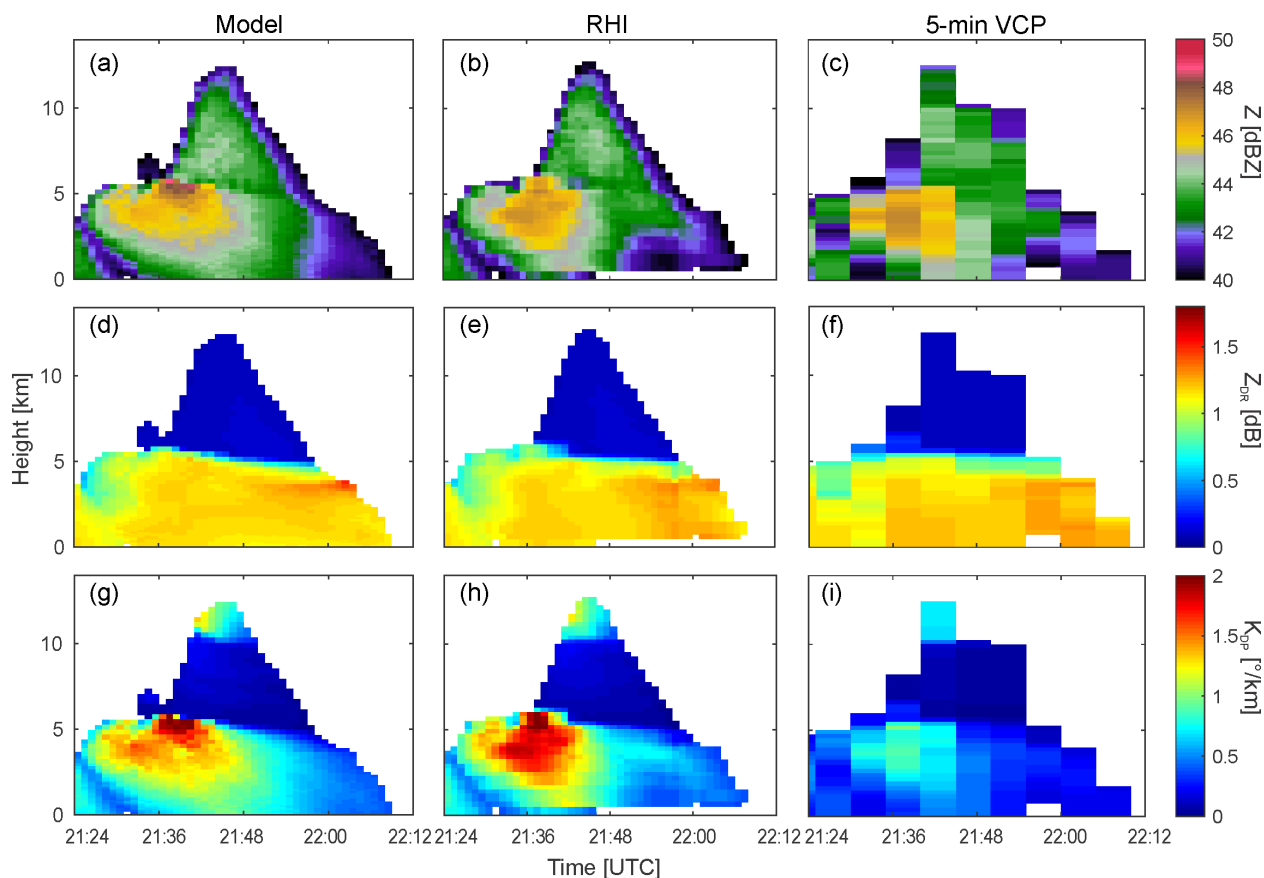
Fig. 5: Time-height cross sections of C-band radar reflectivity (top row), K$_{DP}$ (middle row), and Z$_{DR}$ (bottom row), averaged for areas with reflectivity > 40 dBZ for the selected convective cell for (a,d,g) the model simulation truth, (b,e,h) simulated RHI tracking strategy, and (c,f,i) simulated 5-min volume scan strategy. The cell in this figure is the same as that shown in the box in Fig. 4 and is from the CLN case. Note that the NEXRAD S-band frequency is assumed for the 5-min VCP simulation, while C-band frequency is assumed for the model and RHI simulation. Therefore, the K$_{DP}$ values in this figure include the frequency dependency.
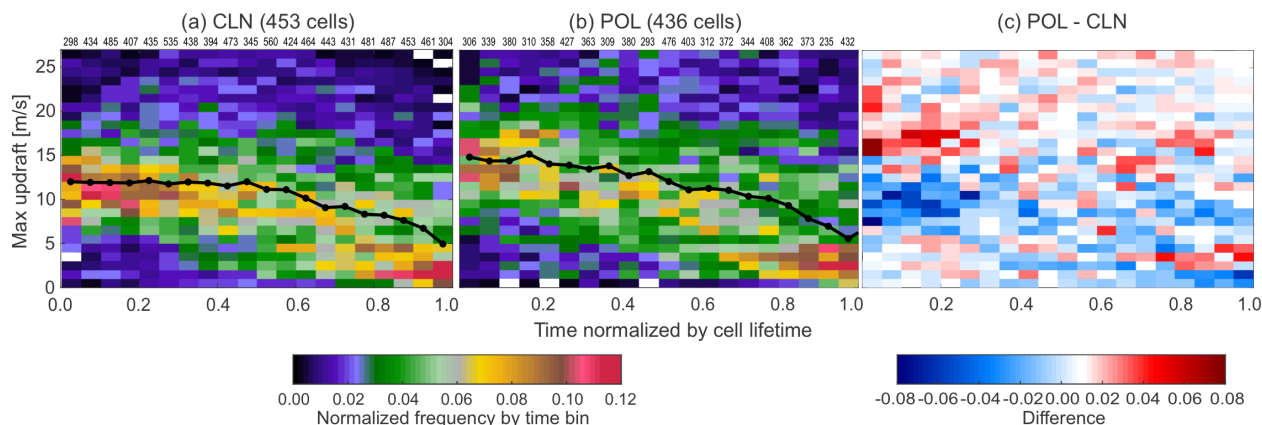
Fig. 6: Frequency of maximum updraft magnitudes in detected individual cells as a function of time normalized by the cell duration for the (a) CLN and (b) POL case simulations, and (c) the difference between the CLN and POL cases (POL – CLN). Here we present only those deep convective cells with 20 dBZ echo top heights that exceeded the freezing level during their lifetimes. Color shading in (a) and (b) represents normalized frequency by cell lifetime, and that in (c) represents the difference in the normalized frequency. The sample size at each time bin is presented on the top of (a) and (b). Black lines in (a) and (b) represent the median value in each time bin.
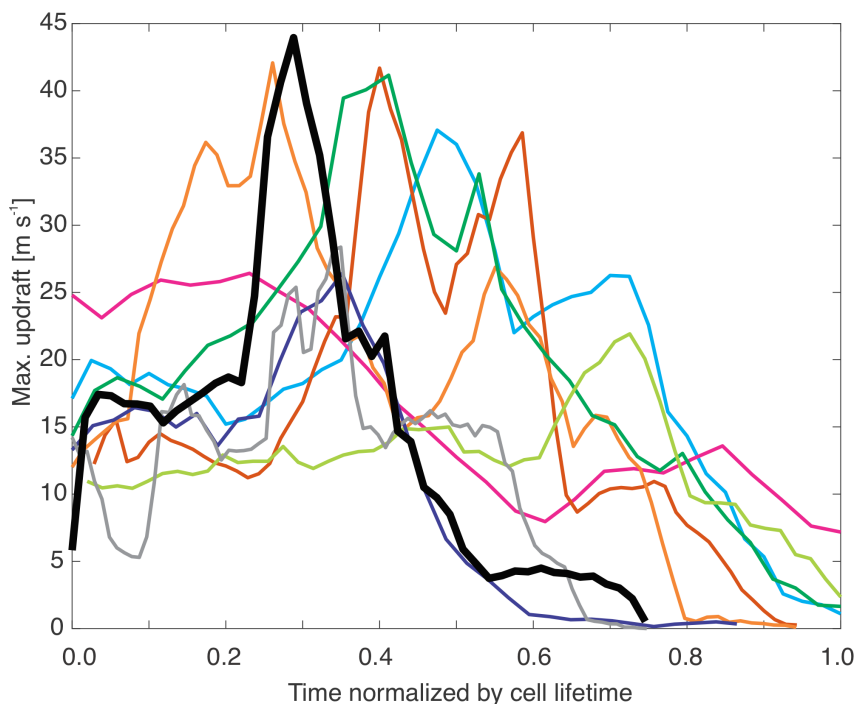
Figure 7: Maximum updraft velocity in the cell column at each time represented as a function of the normalized lifetime for the nine deep convective cells from the CLN simulation. These cells were randomly selected, as described in Section 3.2, and were required to have the maximum radar reflectivity greater than 45 dBZ, the echo top height of 40 dBZ exceeding 5 km in altitude,

645 and the echo top height of 20 dBZ extending above 8 km altitude during the storm lifecycle. The black line represents the target

646 cell that was analyzed for the present OSSE. Note that because the plot displays the maximum updraft found in regions with

647 reflectivity greater than 45 dBZ, some lines do not end at time=1.0 when the maximum reflectivity is below 45 dBZ.

648
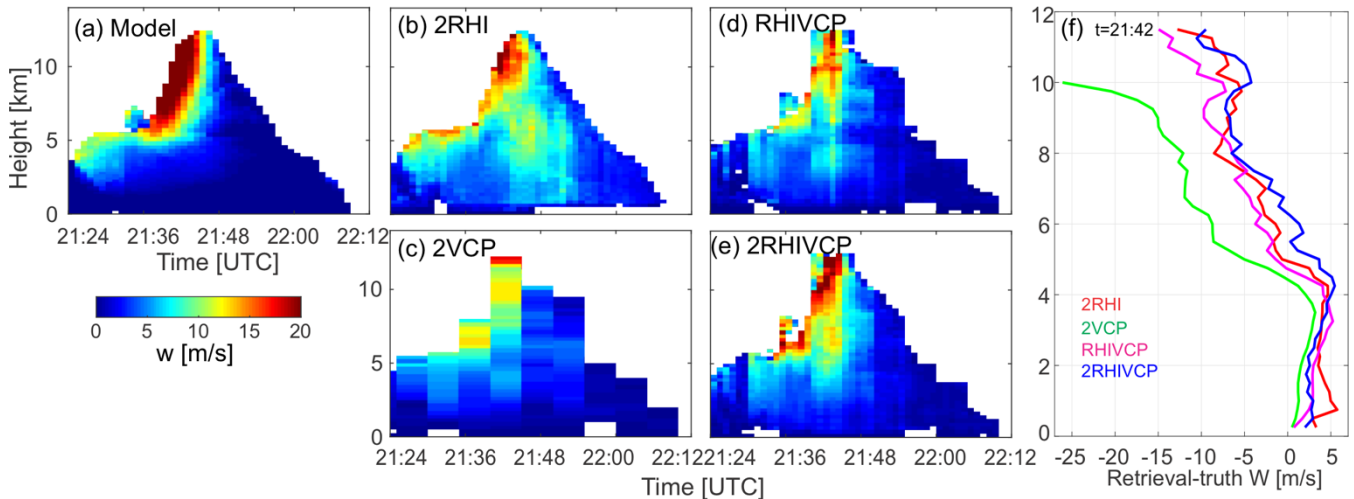
649

650 **Fig. 8: Height-time cross sections of the updraft velocity averaged over the area with reflectivity > 40 dBZ from (a) the model**

651 **(truth) and (b-e) the simulated retrievals, as well as the (f) errors of the simulated multi-Doppler vertical velocity retrievals**

652 **(retrieval - truth) at 21:42 UTC, when the maximum updraft was produced by the cell.**

653

654
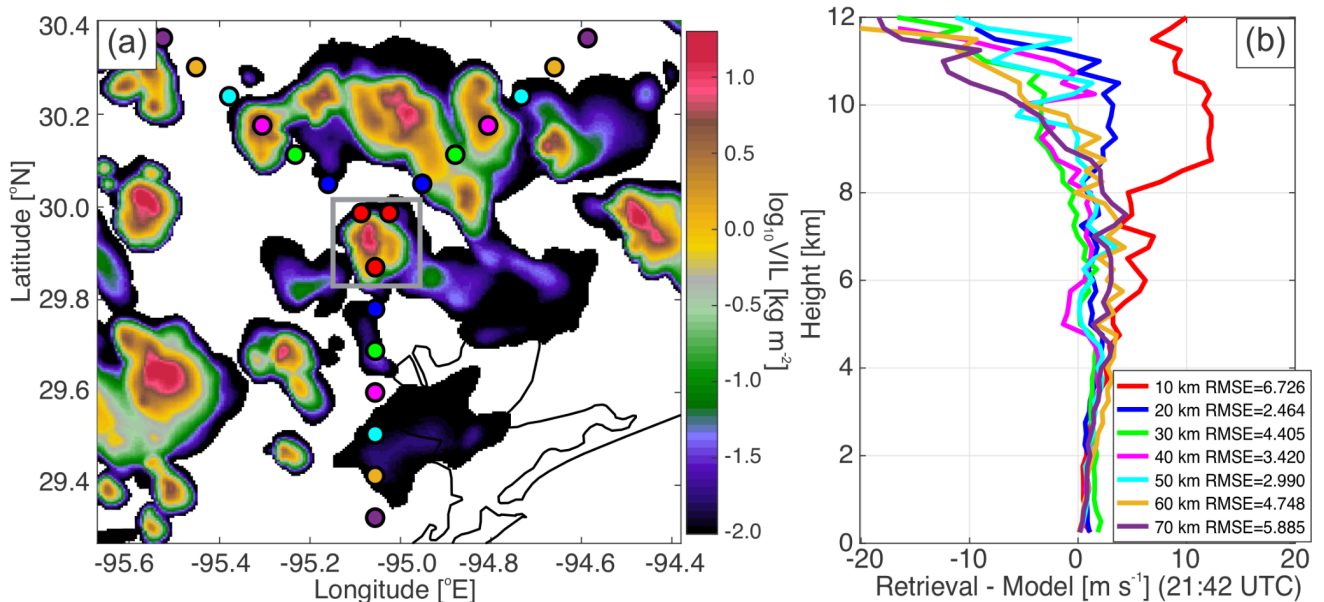
Fig. 9: (a) Horizontal distribution of VIL centered around one identified convective cell (gray box, the same cell shown in Figs. 4, 5, and 8) at 21:42 UTC from the CLN simulation and (b) vertical profiles of errors of simulated retrievals (retrieval - model) averaged over a 20 km x 20 km box with reflectivity > 30 dBZ at 21:42 UTC for the identified convective cell. The colored dots in (a) represent the radar locations for the multi-Doppler radar wind retrievals. The colors of the dots correspond to the colors of the set of the radars for the multi-Doppler radar wind retrievals shown in (b). The two radars to the north of the cell performed 2-min RHIs, and the other performed 5-min VCP. The RMSE for each profile is displayed in (b).
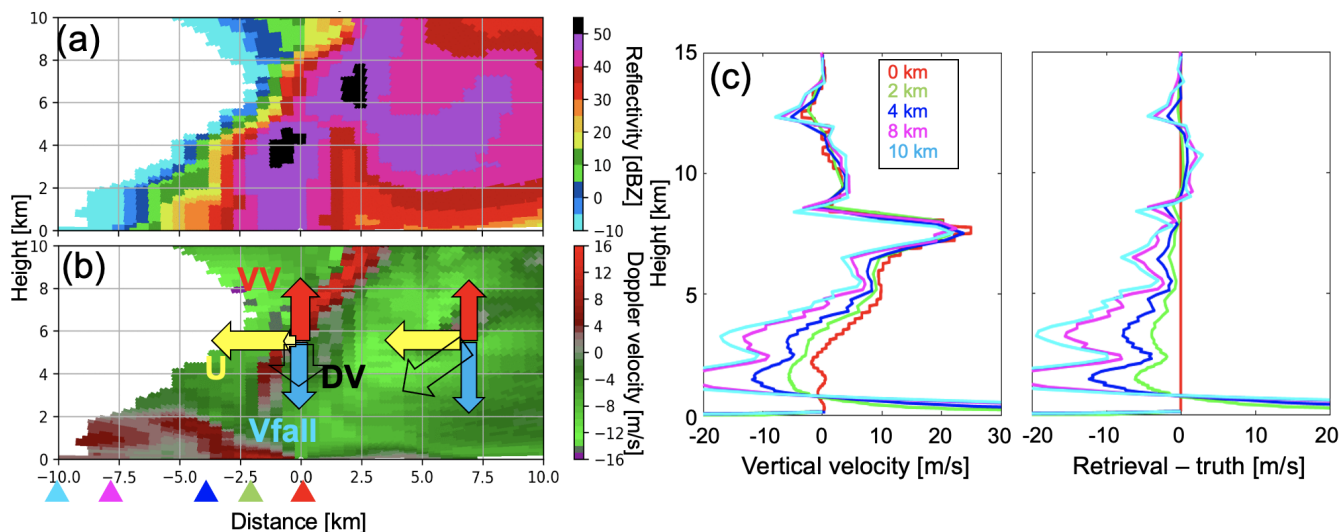
Fig. 10: Vertical cross section of (a) radar reflectivity and (b) Doppler velocity from the simulated RHI measurement for a convective cell and vertical profiles of (c) retrieved vertical air motion and (d) errors (retrieval – model), simulated with different distances between the radar and the center of the convective cell (distance = 0 km in b) at 21:42 UTC. The location of the radars from the center of the convective cell in (c-d) are indicated by their corresponding colored triangle in panel (b). A negative Doppler velocity in (b) represents motion toward the radar.
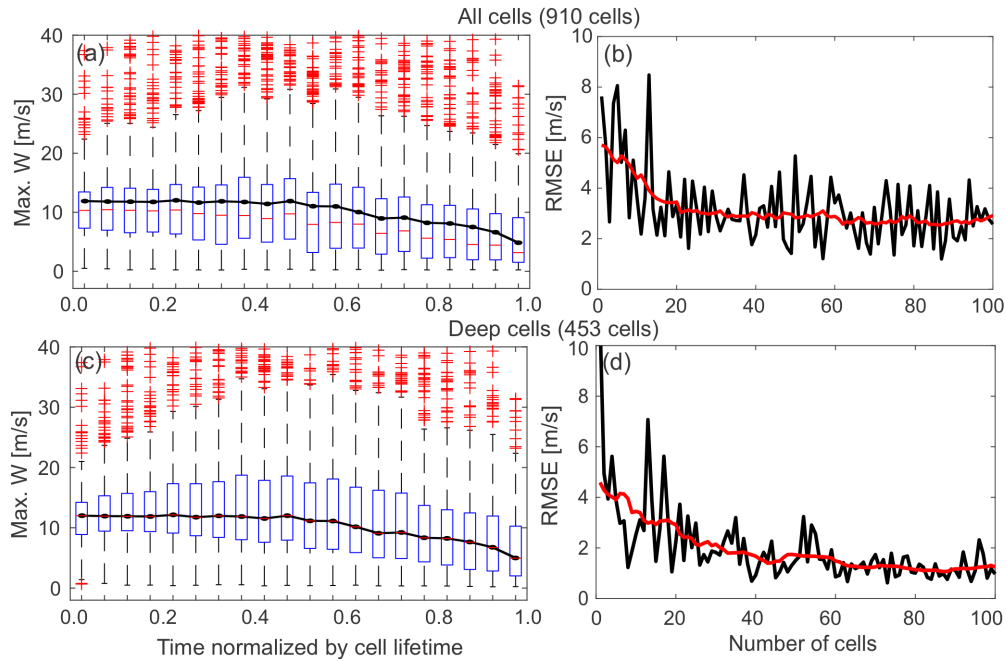
Figure 11: (a,c) Boxplots of maximum vertical velocity as a function of the normalized lifetime from all convective cells detected (910 cells including deep and shallow cells) from the CLN case and from the deep convective cells (453 cells) defined in Fig. 6a, respectively. For each boxplot, the central red mark indicates the median, and the bottom and top edges of the box indicate the 25th and 75th percentiles, respectively. The whiskers extend to the most extreme data points excluding outliers. Outliers are plotted individually using the cross symbol. Black solid lines in (a) and (c) represent the temporal evolution of the median values of maximum updrafts for deep cells as a function of time. (b,d) The RMSEs of median values of the maximum vertical velocity as a function of the number of cells randomly sampled from all convective cells detected in the CLN simulation (b) and from deep convective cells defined in Fig. 6a (d). The RMSEs are estimated from the median profiles as a function of the normalized lifetime from the random sampling and that from the all deep convective cells (black line in Fig. 6a).
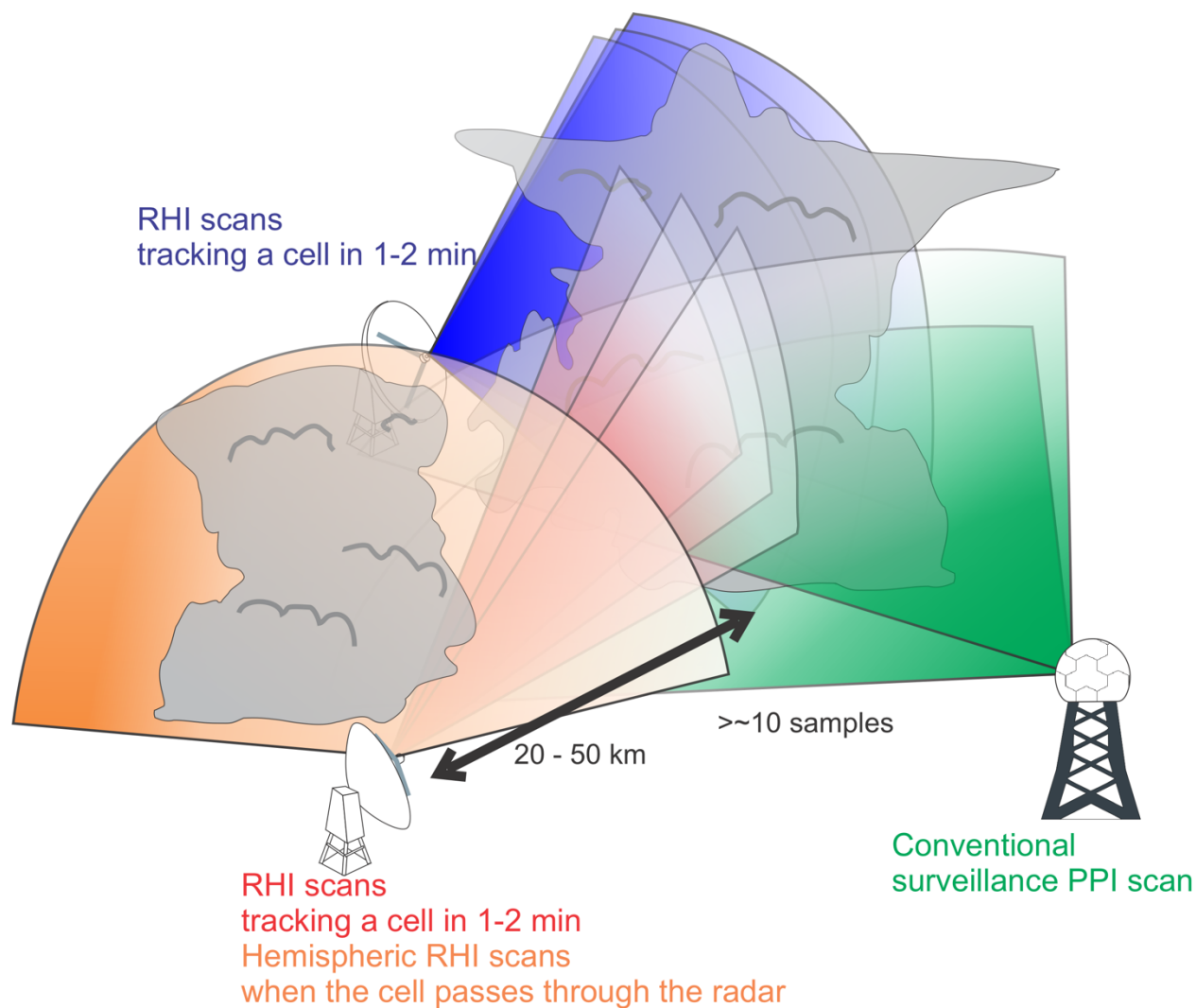
Figure 12: A schematic image of a suggested scan strategy optimized for observing convective cell evolution. Optimal cell tracking is achieved by frequent RHI scans from more than one radar (blue and red scans) in addition to the operational PPI volume scans generally performed by the NEXRAD radars (green scans). The schematic also suggests an optimal hybrid radar scan strategy which switches between cell tracking by frequent RHI measurements and hemispheric RHI measurements depending on the distance between the radar and the target cell (red and orange scans).